

# Induced transparency by coupling of Tamm and defect states in tunable terahertz plasmonic crystals

Gregory C. Dyer<sup>1\*</sup>, Gregory R. Aizin<sup>2</sup>, S. James Allen<sup>3</sup>, Albert D. Grine<sup>1</sup>, Don Bethke<sup>1</sup>, John L. Reno<sup>1</sup> and Eric A. Shaner<sup>1\*</sup>

**Photonic crystals and metamaterials have emerged as two classes of tailorable materials that enable the precise control of light. Plasmonic crystals, which can be thought of as photonic crystals fabricated from plasmonic materials, Bragg scatter incident electromagnetic waves from a repeated unit cell. However, plasmonic crystals, like metamaterials, are composed of subwavelength unit cells. Here, we study terahertz plasmonic crystals of several periods in a two-dimensional electron gas. This plasmonic medium is both extremely subwavelength ( $\sim \lambda/100$ ) and reconfigurable through the application of voltages to metal electrodes. Weakly localized crystal surface states known as Tamm states are observed. By introducing an independently controlled plasmonic defect that interacts with the Tamm states, we demonstrate a frequency-agile electromagnetically induced transparency phenomenon. The observed 50% *in situ* tuning of the plasmonic crystal band edges should be realizable in materials such as graphene to actively control plasmonic crystal dispersion in the infrared.**

Photonic bandgaps<sup>1</sup>, strong light–matter interaction<sup>2</sup>, slow light<sup>3</sup> and negative refractive index<sup>4</sup> arise in photonic-crystal structures<sup>5,6</sup> due to Bragg scattering of electromagnetic waves from a repeated unit cell. Generally, the electromagnetic properties of photonic crystals engineered from bulk semiconductors, metals and dielectrics are only weakly tunable, if at all. Material systems such as two-dimensional electron gases (2DEGs) embedded in semiconductors<sup>7,8</sup> and graphene<sup>9–11</sup> offer a substantially more flexible electromagnetic medium. These plasmonic materials can be lithographically patterned and electronically tuned, giving rise to a variety of subwavelength plasmonic devices that may be broadly controlled via an applied d.c. electric field. When a periodic structure is engineered from these systems, a plasmonic band structure can be realized<sup>12–15</sup>. The 2DEG and graphene thus provide a platform for the exploration of widely tunable plasmonic bandgap structures.

Subwavelength plasmonic media that utilize a 2DEG formed at a GaAs/AlGaAs interface are the central focus of this article. Similar to the  $\omega$ - $q$  plasmon dispersion in graphene, the 2DEG plasmon dispersion depends explicitly upon both the plasmon wavevector and the a.c. conductivity of the medium. An effective methodology to describe plasma excitations in a 2DEG is that of an ‘LC’ plasmonic resonator<sup>16</sup>. Here,  $L$  is the field-effect tunable kinetic inductance of the 2DEG. The 2DEG capacitance can be introduced as

$$C = 2q\varepsilon_{\text{eff}} \quad (1)$$

where  $\varepsilon_{\text{eff}}$  is the effective permittivity of the embedded 2DEG and  $q$  is the plasmon wavevector<sup>14,17–19</sup>. In high-mobility 2DEG materials at microwave and terahertz frequencies, underdamped ‘LC’ plasma resonances are supported, allowing for propagation lengths on the order of tens of micrometres or plasmon wavelengths.

The introduction of spatial periodicity to a 2DEG produces a plasmonic crystal where the 2DEG is a coherent plasmonic medium. Although a plasmonic crystal is physically more similar to a photonic crystal than a metamaterial, the unit cell of a 2DEG plasmonic crystal is deeply subwavelength. These tunable plasmonic materials are conceptually related to certain periodic plasmonic nanostructures<sup>20</sup>, resonant microwave metalenses<sup>21</sup> and acoustic metamaterials<sup>22</sup>. In such systems, band structure results from incident waves interacting with spatially periodic subwavelength resonant scatterers<sup>23,24</sup>.

## 2DEG plasmonic crystals

In this Article, we examine the complex interplay between surface states known as Tamm states<sup>25</sup>, plasmonic defect modes, and the plasmonic crystal band structure in tunable terahertz plasmonic bandgap devices engineered from a GaAs/AlGaAs 2DEG. The studied plasmonic crystal devices, samples A and B, are presented in Fig. 1a,b. Both are integrated at the vertex of an antenna with bandwidth from 100 GHz to 1 THz. These plasmonic structures are based upon a four-period plasmonic crystal formed below gate G1, with an adjacent independently controlled plasmonic defect<sup>26,27</sup> controlled by gate G2. A plasmonic defect is induced when G2 is tuned to a different voltage from G1. Although these plasmonic bandgap structures are nearly 100 times smaller than the free-space wavelength of terahertz radiation, they cannot be considered an effective medium because the wavelengths of the terahertz plasmons tightly confined to the 2DEG are comparable to the size of the plasmonic crystal unit cell<sup>28,29</sup>.

The adjacent regions of 2DEG in this system can be represented as sequential distributed plasmonic ‘RLC’ transmission line elements, where  $C$  is defined in equation (1). It is convenient to treat the plasmonic crystal unit cell using this equivalent circuit approach as illustrated in Fig. 1c. In Fig. 1d, the plasmonic crystal unit cell is indicated

<sup>1</sup>Sandia National Laboratories, PO Box 5800, Albuquerque, New Mexico 87185, USA, <sup>2</sup>Kingsborough College, The City University of New York, Brooklyn, New York 11235, USA, <sup>3</sup>Institute for Terahertz Science and Technology, UC Santa Barbara, Santa Barbara, California 93106, USA. \*e-mail: gcdyer@sandia.gov; eashane@sandia.gov

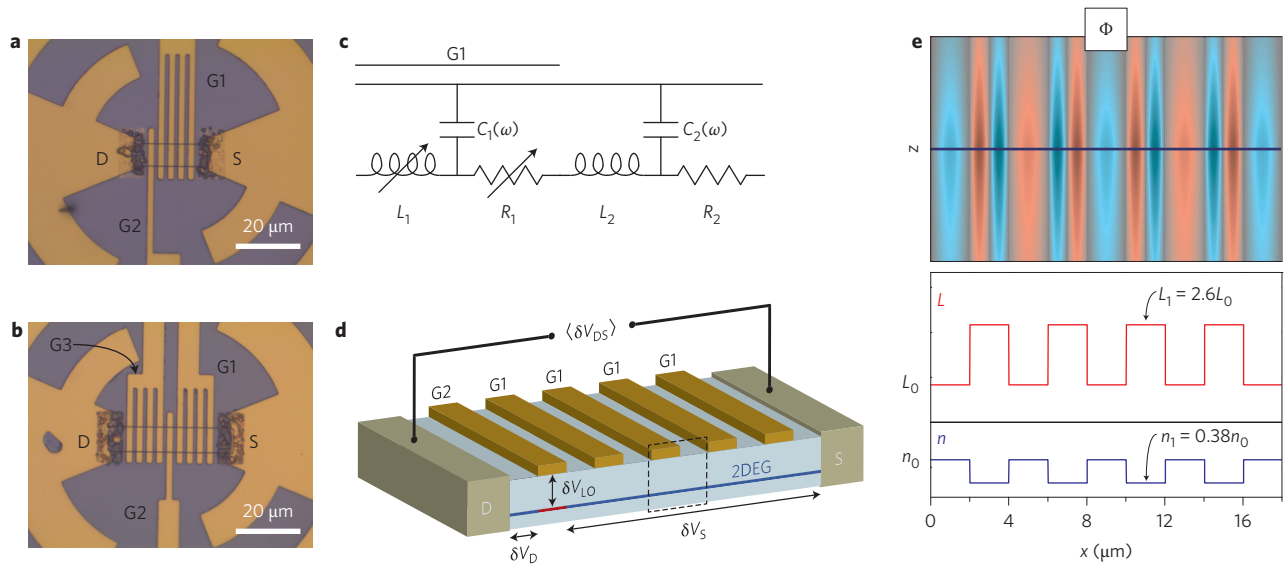


**Figure 1 | Integrated plasmonic crystal structures.** **a, b**, Images at the broadband antenna vertex of sample A (**a**) and sample B (**b**) are shown with gates (G1 and G2 for both samples, G3 for sample B only), source (S) and drain (D) terminals labelled. **c**, Equivalent distributed circuit for the plasmonic crystal unit cell with ungated and gated region elements below G1. **d**, Diagram of sample A, illustrating the coupling of fields to the plasmonic mixer induced below G2 with the depleted region shown in red and the 2DEG indicated by the blue line. The photovoltage is measured between D and S terminals. **e**, Distribution in the  $x$ - $z$  plane of the potential  $\Phi$  near the plane of the 2DEG is plotted for a resonance ( $L_1 = 2.6 L_0$ ,  $\nu = 456$  GHz) of the plasmonic crystal formed between G2 and S. The plane of the 2DEG is indicated by a dark blue line. Shown below are the equilibrium 2DEG inductance  $L$  (red) and density  $n$  (blue) of the plasmonic crystal.

by a dashed box in a cross-sectional illustration of sample A. The kinetic inductance  $L$  and resistance  $R$  of the equivalent distributed circuit are explicitly defined through the Drude conductivity of the 2DEG,  $\sigma(\omega)^{-1} = R + i\omega L$  (refs 16,30; Supplementary Section SI).

Tuning of gate voltages G1 and G2 controls the 2DEG inductance and resistance,  $L_j, R_j \propto 1/\gamma_j$ . Here,  $\gamma_j$  defines the normalized 2DEG density in terms of the threshold voltage  $V_{th}$  (where  $n_{2D} \rightarrow 0$ ) and the applied gate voltages  $V_{Gj}$  such that  $\gamma_j \equiv (V_{th} - V_{Gj})/V_{th}$ . In terms of the plasmonic crystal unit cell described in Fig. 1c, the applied gate voltage  $V_{G1}$  controls the inductance  $L_1$  and resistance  $R_1$ . The ungated region of the 2DEG has constant distributed inductance  $L_0$  and resistance  $R_0$ .

In Fig. 1e, the electric potential  $\Phi$  of a plasma wave of frequency  $\nu = 456$  GHz is illustrated in a four-period plasmonic crystal. The potential  $\Phi$  is shown around the plane of the 2DEG. Also indicated are the spatially periodic equilibrium 2DEG kinetic inductance  $L$  and density  $n$  of the four-period plasmonic crystal. Here, a  $2 \mu\text{m}$  plasmon wavelength below G1 is evident for the 456 GHz excitation with free-space wavelength of  $658 \mu\text{m}$ , or approximately  $\lambda/300$ .

### Active control of plasmonic band structure

To develop intuition concerning the tunability of the plasmonic crystal, we first considered the bulk plasmonic band structure of a plasmonic crystal with an infinite number of periods. The crystal dispersion of the infinite plasmonic crystal, plotted in Fig. 2a for several values of  $\gamma_1$ , was calculated from the one-dimensional Kronig-Penney model<sup>19</sup> for the unit cell shown in Fig. 1c:

$$\cos(2k_B a) = \cos(q_1 a) \cos(q_0 a) - \frac{1}{2} \left( \frac{Z_1}{Z_0} + \frac{Z_0}{Z_1} \right) \sin(q_1 a) \sin(q_0 a) \quad (2)$$

where  $k_B$  is the Bloch wavevector,  $q_j$  and  $Z_j$  are the plasmon wavevector and characteristic impedance, respectively, of the two elements forming the unit cell, and  $a$  is the length of the  $j$ th section of 2DEG (Supplementary Section SII). With  $\gamma_1 = 0.8$ , minigaps begin to emerge in the 2DEG plasmon dispersion relation that is

folded into the first Brillouin zone. As  $\gamma_1$  further decreases, full plasmonic bandgaps are evident and the entire band structure shifts downward in frequency.

A four-period plasmonic crystal between S and G2 can be induced in sample A (shown in Fig. 1a) by biasing the defect gate G2 past its threshold voltage, as illustrated in Fig. 1d. The plasmonic crystal formed below G1 delivers a plasmonic signal to a rectifying detection element under G2, generating a photovoltage  $\langle \delta V_{DS} \rangle$  as explained in the Methods. By tuning G1 and frequency as plotted in Fig. 2b, the measured photoresponse maps the plasmonic spectrum of sample A. The bright regions correspond to the resonant excitation of plasma modes in the system (Supplementary Section SII). For comparison, resonant modes calculated for the four-period plasmonic crystal using a transfer matrix formalism<sup>14,19</sup> (Supplementary Section SI) are shown by solid lines. These eight resonances are associated with the second and third allowed bands, and the five lowest orders of these resonances are resolved experimentally. Above 350 GHz and  $V_{G1} < -2.00$  V, discrete modes cannot be resolved due to the relatively shorter plasmon coherence length in this regime (Supplementary Section SIII).

Each unit cell of the four-period structure would have an identical resonant frequency in isolation. However, the coherence of the plasma wave across the plasmonic crystal lifts this fourfold degeneracy, resulting in the formation of four state bands. Alternatively, this can be considered a Fano-type system where interference between a continuum, the allowed bands of the plasmonic crystal, and the discrete modes of the cavity formed between S and G2 produces groups of four asymmetric resonances<sup>24</sup>. These bands of states are demonstrated in Fig. 2a to tune a minimum of 50% in frequency from 300 GHz to 450 GHz, although in principle the shift of the bandgap can be well in excess of 100%.

The first three experimentally observed resonances in Fig. 2b, moving from the lower right-hand corner (300 GHz and  $V_{G1} = 0.00$  V) towards the upper left-hand corner, are positioned in an allowed infinite plasmonic crystal band. These band states are highlighted in blue. However, the fourth mode associated with this band is largely found in the second bandgap of the infinite

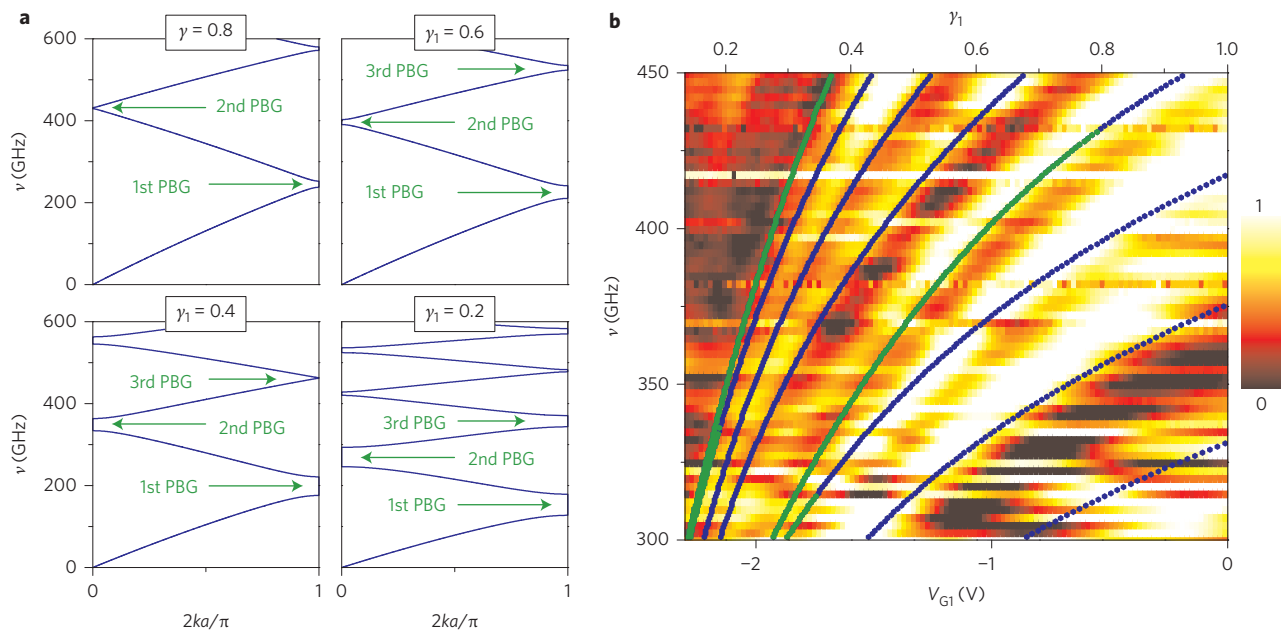


**Figure 2 | Tunable plasmonic crystal spectrum.** **a**, Frequency-wavevector dispersion of the plasmonic crystal based on the unit cell in Fig. 1c, plotted for  $\gamma_1 = 0.8, 0.6, 0.4$  and  $0.2$ . Only positive wavevectors are shown. **b**, Self-normalized plasmonic crystal photovoltage spectrum of sample A plotted as a function of  $V_{G1}$  and frequency. Eight calculated plasmonic crystal modes are shown in blue, with sections of the modes that are found in the infinite crystal bandgap indicated in green.

plasmonic crystal, where it is highlighted in green. All regions of modes highlighted in green are in the predicted bandgaps corresponding to those labelled in Fig. 2a, including a pair near  $V_{G1} = -1.80$  V and 300 GHz. These modes could potentially represent plasmonic Tamm states<sup>19,25</sup>. Tamm states, weakly localized crystal surface states with a complex rather than purely real Bloch wavevector ( $\text{Im}[k_B] \neq 0$ ), are generally found in a bandgap and have been experimentally demonstrated only in a few electronic<sup>31</sup>, photonic<sup>32</sup> and hybrid optical-plasmonic<sup>33</sup> systems. In contrast to surface states resulting from dislocations and impurities, Tamm states form at the ideal termination of a lattice and are most easily isolated in tailorable structures like semiconductor superlattices and photonic crystals. Although the results shown in Fig. 2 are indicative of Tamm state formation, additional direct measurements are needed to justify this hypothesis.

### Evidence of plasmonic Tamm states

To search for Tamm states in this system, sample B (Fig. 1b) was studied with gate G3 biased beyond its threshold voltage. Here, the last stripe of depleted 2DEG below G3 operates as a rectifying detector, as illustrated in Fig. 3a (Supplementary Section SII). This configuration of sample B provides a means to study the strong coupling between the four-period plasmonic crystal below G1 and the plasmonic defect<sup>26,27,34</sup> defined under G2. The photoreponse to excitation frequencies of 302.5, 363.0 and 420.5 GHz as G1 and G2 are independently tuned is shown in Fig. 3b,d,f, respectively. As in Fig. 2b, the bright regions represent plasma resonances. In Fig. 3c,e,g the calculated plasmonic crystal-defect structure plasmon modes (blue lines) are plotted for these same frequencies as a function of normalized 2DEG densities  $\gamma_i$  corresponding to the experimentally applied gate voltages. The bandgaps of the infinite plasmonic crystal where the Bloch wavevector of experimentally observed resonances has a non-zero imaginary component are indicated in grey.

An understanding of the relationship between the plasmonic crystal and plasmonic defect states emerges when considering Fig. 3b–g. The four-period plasmonic crystal modes are tuned by

$G1$  and appear as vertical features when the plasmonic defect is not resonating. Plasmonic defect resonances are modes controlled by  $G2$  and appear as bright horizontal lines where sequential anti-crossings occur. When  $V_{G1} = V_{G2}$ , the plasmonic defect may be viewed as a fifth identical unit cell that is appended to the four-period plasmonic crystal under  $G1$ . This condition is satisfied along the diagonal lines in Fig. 3b–g where a fifth discrete mode is added to each band by a higher-order mode moving into a lower energy band after traversing the infinite plasmonic crystal bandgap.

The black boxes in Fig. 3b–e highlight repelled crossings between two states in or near the second bandgap along the diagonal line  $V_{G1} = V_{G2}$ . A repelled crossing is found along this diagonal if and only if a plasmonic defect and a Tamm state of the same order are mutually coupled. Because an isolated plasmonic defect state is localized, it must enter into a bandgap before joining a five-state band as an orthogonal plasmonic crystal mode. Only localized states are found in the infinite plasmonic crystal bandgap. A Tamm state bound near the ohmic contact is the only viable candidate to cross with a plasmonic defect mode along the line  $V_{G1} = V_{G2}$ .

There are several additional distinctions between crossings of the plasmonic defect modes with purely real-valued Bloch wavevector plasmonic crystal states and with complex Bloch wavevector Tamm states. Modes in the allowed bands are completely delocalized and are therefore widely separated as they come into resonance with a plasmonic defect mode. In Fig. 3f,g under 420.5 GHz excitation where the bandgaps largely vanish, none of the plasmonic crystal states becomes localized and for any fixed choice of  $V_{G1}$  ( $\gamma_1$ ) the resonances are widely spaced in  $V_{G2}$  ( $\gamma_2$ ). In contrast, due to the localization of Tamm states, both their coupling with the plasmonic defect and the size of the plasmonic defect–Tamm splitting are comparatively smaller. This leads to the close approach of the modes in the black boxed regions of Fig. 3b–e.

### Plasmon-induced transparency

As the energy of a plasmonic defect mode approaches that of the Tamm state by tuning  $V_{G2} \rightarrow V_{G1}$ , an analogy may be drawn to

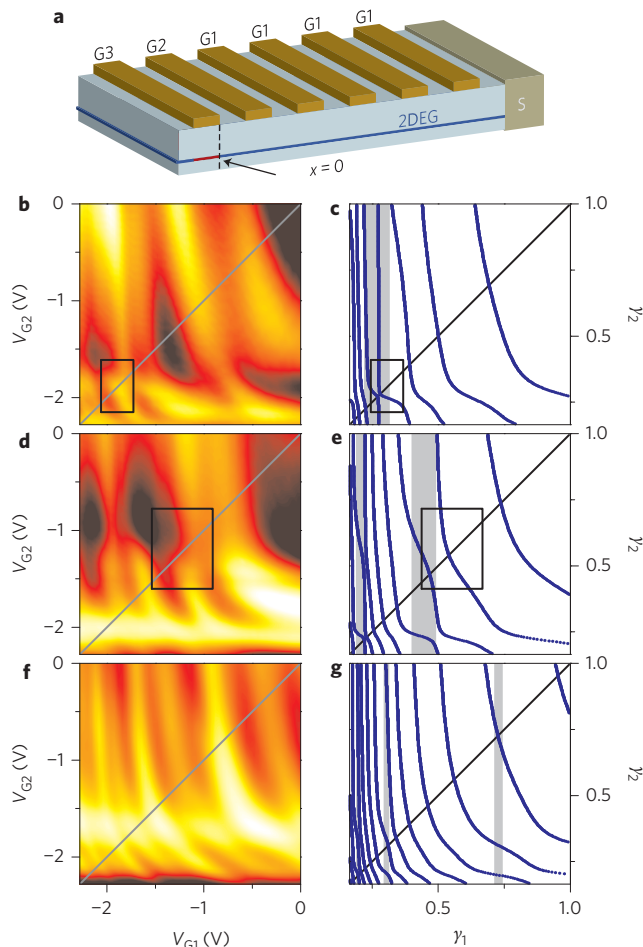


**Figure 3 | Tamm states in plasmonic crystal defect structures.** **a**, Schematic of sample B configured such that a four-period plasmonic crystal, tuned by G1, with adjacent plasmonic defect, tuned by G2, is formed between S and G3. The plasmonic detection region is indicated in red. Plots of the plasmonic photovoltage spectra of sample B as a function of  $V_{G1}$  and  $V_{G2}$  are shown for 302.5 GHz (**b**), 363.0 GHz (**d**) and 420.5 GHz (**f**) excitation frequencies. The calculated bandgaps (grey) of the infinite plasmonic crystal and the plasmonic crystal-plasmonic defect system modes (blue) are plotted for 302.5 GHz (**c**), 363.0 GHz (**e**) and 420.5 GHz (**g**).

electromagnetically induced transparency (EIT)<sup>35–37</sup>, provided several conditions are satisfied. The description of EIT in classical systems is that of two coupled oscillators, one of which is ‘bright’ and the other ‘dark’ with respect to incident radiation. In this picture, the plasmonic defect and Tamm states must then be coherently coupled and resonate at the same frequency, conditions that are satisfied empirically in this plasmonic system. More importantly, there must be an asymmetry in both the external coupling and the damping rates of the coupled plasmonic oscillators. The ‘dark’ resonance must be weakly externally coupled and have a higher quality factor than the ‘bright’ resonance. In high-quality 2DEG plasmonic systems, weak coupling to an external excitation implies a higher ‘Q’ resonance, because radiative damping is the dominant dissipation mechanism of the plasmon (Supplementary Section SIII).

This plasmonic EIT-like effect is studied through analysis of the plasmonic crystal-plasmonic defect modes in and near the first bandgap. Although it is common to sweep frequency in order to map the interaction of strongly coupled resonators<sup>38</sup>, our approach of tuning resonators *in situ* with fixed excitation frequency yields the same information. Figure 4a shows the photoresponse of sample B with an excitation frequency of 210.0 GHz. Here, the characteristic

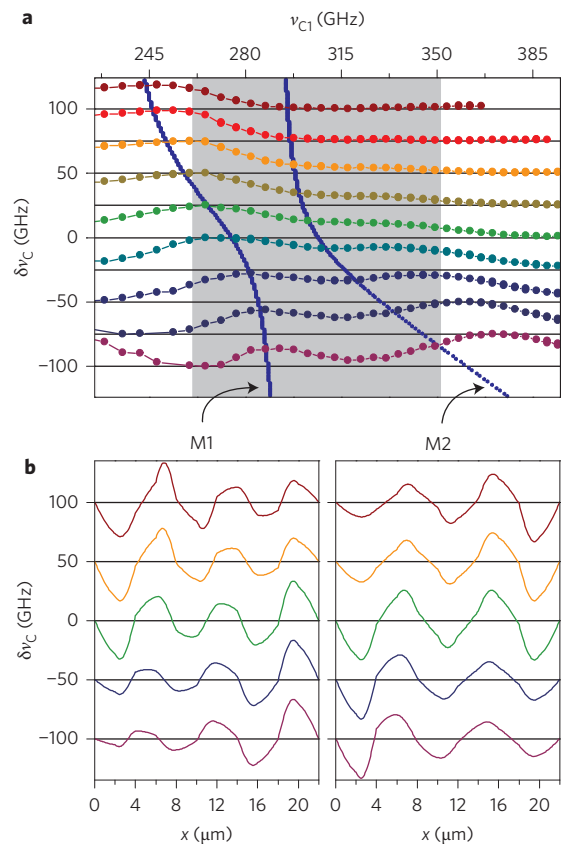


**Figure 4 | Induced transparency in the first plasmonic bandgap.** **a**,

Normalized photovoltage as a function of the plasmonic crystal characteristic frequency shown for 210.0 GHz excitation. Each curve corresponds to a different detuning of the plasmonic defect characteristic frequency relative to that of the plasmonic crystal unit cell from –100 to +100 GHz in 25 GHz steps. The calculated modes are plotted in blue with bandgaps shaded in grey. The arrows highlight modes denoted M1 and M2. **b**, Spatial voltage distributions in the plane of the 2DEG for M1 and M2, with several detunings plotted, highlighting the interaction of plasmonic defect and Tamm states under 210.0 GHz excitation.

frequency  $\nu_{C1}$  of the plasmonic crystal unit cell is swept for different detunings  $\delta\nu_C$  of the plasmonic defect relative to the plasmonic crystal unit cell. The characteristic plasma frequencies

$$\nu_{Cj} = \beta_C / 2\pi \sqrt{L_j C_j} \quad (3)$$

are defined for the plasmonic crystal unit cell ( $j = 1$ ) and plasmonic defect ( $j = 2$ ) using the fundamental wavevector  $\beta_C \equiv \pi/a$  of the plasmon mode confined below an  $a = 2 \mu\text{m}$  wide gate finger. In fact, the characteristic frequencies  $\nu_{Cj}$  are the fundamental plasma frequencies of the isolated plasmonic crystal unit cell and plasmonic defect. The detuning of the plasmonic defect characteristic frequency from that of the plasmonic crystal unit cell is given by  $\delta\nu_C = \nu_{C2} - \nu_{C1}$ . These definitions of  $\nu_{Cj}$  parameterize the strong coupling behaviour of the plasmonic crystal-plasmonic defect system.

For positive detunings  $\delta\nu_C > 50$  GHz, an asymmetric resonance associated with the plasmonic defect is observed at the edge of the bandgap (shaded grey) in Fig. 4a, while the Tamm state appears inert due to its poor coupling to both the incident terahertz field and the integrated detector. Here, we interpret the plasmonic defect as a ‘bright’ resonator that, under appropriate conditions, can couple to and drive the ‘dark’ Tamm state. The plasmonic defect and Tamm states become strongly interacting when the



detuning is reduced,  $-50 \text{ GHz} \leq \delta\nu_C \leq +50 \text{ GHz}$ . As the energetic difference between these states decreases, the 'bright' plasmonic defect excites the formerly 'dark' Tamm state. A characteristic signature of EIT, a symmetric double peak with a dip at its centre, is evident in Fig. 4a with the detuning set to  $\delta\nu_C = -50 \text{ GHz}$ . For negative detunings  $\delta\nu_C < -50 \text{ GHz}$ , the plasmonic defect state shifts to larger characteristic frequencies  $\nu_{C1}$ , and the amplitude of the Tamm state decreases. The calculated modes, shown in blue in Fig. 4a, agree well with the measurements.

The plasmonic spatial distributions in Fig. 4b highlight the evolution of the plasmonic defect and Tamm states. The distributions of modes M1 and M2, indicated by the arrows linking to Fig. 4a, are plotted for several detunings  $\delta\nu_C$ . The position corresponds directly to Fig. 3a; the mixer edge is at  $x = 0$ , the plasmonic defect is located in  $2 < x < 4$ , and the plasmonic crystal is found in  $6 < x < 22$ . Both the 'bright' plasmonic defect state, seen distinctly with  $\delta\nu_C > 0$  for M1 and  $\delta\nu_C < 0$  for M2, and the 'dark' Tamm state, observed with  $\delta\nu_C < 0$  for M1 and  $\delta\nu_C > 0$  for M2, are weakly localized. For  $\delta\nu_C = 0$ , the crystal is sufficiently short that the spatial overlap of the two weakly localized states lifts their degeneracy. Plasmonic crystal modes develop around zero detuning that are analogous to bonding and antibonding states. These may also be interpreted as coupled Tamm states formed at opposing edges of the plasmonic crystal<sup>19,39,40</sup>.

## Conclusions and outlook

In this Article, we have studied the band structure as well as coupled surface and defect states in tunable plasmonic crystal structures. The engineering of plasmonic resonators *in situ* rather than solely through lithographic tuning of the physical geometry opens a previously unexplored avenue for the study of strongly coupled electromagnetic systems<sup>38</sup>. Both photonic crystals<sup>3</sup> and coupled resonators<sup>35,41</sup> can be harnessed for slow light applications, and tunable plasmonic systems provide a useful degree of freedom for possible slow light devices. Although the presented plasmonic devices based upon GaAs/AlGaAs heterostructures are probably limited in both operating temperature ( $< 77 \text{ K}$ ) and operating frequency ( $< 1 \text{ THz}$ ), both GaN-based 2DEGs and graphene<sup>42</sup> hold promise for extending the viable range of the plasmonic crystal-based structures (Supplementary Section SIV). Recent studies have shown tunable terahertz plasmons in GaN 2DEGs at  $170 \text{ K}$  (ref. 43) and at room temperature in graphene<sup>9,10</sup>, as well as mid-infrared plasmons in graphene nanostructures<sup>44,45</sup>. Finally, we note that manipulation of the localized plasmonic crystal defect and Tamm state field distributions to produce strong field enhancements<sup>27</sup> in 2DEG structures could give rise to a new generation of ultrasensitive direct and heterodyne terahertz detectors as well as terahertz oscillators<sup>46</sup>.

## Methods

The devices were fabricated using standard contact lithography, metallization deposition and liftoff techniques from a GaAs/AlGaAs double quantum-well heterostructure (Sandia wafer EA1149) with total 2DEG density of  $4.02 \times 10^{11} \text{ cm}^{-2}$  at  $12 \text{ K}$ . The 2DEG was embedded a distance  $d = 386 \text{ nm}$  below the surface of the molecular beam epitaxy-grown heterostructure. The periodic gates were designed to have a  $4.0 \text{ }\mu\text{m}$  period with a 50% metallization duty cycle, while the fabricated dimension differed slightly, yielding a  $3.8 \text{ }\mu\text{m}$  period with  $\sim 60\%$  metallization duty cycle of the  $10\text{-}\mu\text{m}$ -wide mesa. The terahertz radiation was generated with a Virginia Diodes (VDI) microwave frequency multiplication chain and optically coupled through z-cut quartz windows in a closed-cycle cryogenic system. Photoresponse and transport measurements were performed at  $75 \text{ Hz}$  modulation rate using a Stanford Research 830 lock-in amplifier to measure the voltage between source and drain terminals.

A purely electronic approach was used to probe the plasmonic bandgap structures. Depletion of the 2DEG ( $n_{2D} \rightarrow 0$ ) below a gate allows for conversion of plasma waves into a measurable photoresponse<sup>8,26</sup> that can have both photoconductive<sup>47</sup> and photovoltaic<sup>34</sup> contributions. In this work, the distributed terahertz excitation of the device terminals produces a plasmonic homodyne mixing response<sup>48–50</sup> measured between the drain (D) and source (S) contacts, as illustrated for sample A in Fig. 1d. The local oscillator voltage  $\delta V_{LO}$  is coupled from

G2 to the region of depleted 2DEG below, while the signal coupled to the mixer is the difference between the plasmonic voltages  $\delta V_D - \delta V_S$  generated on either side of the depletion region. A nonlinear plasmonic mixing mechanism in the region of depleted 2DEG downconverts the component of the differential terahertz signal  $\delta V_D - \delta V_S$  in phase with  $\delta V_{LO}$  to a photovoltage  $\langle \delta V_{DS} \rangle$  (Supplementary Section SII).

The threshold voltage  $V_{th}$  of both devices was found using standard lock-in techniques to measure transistor channel conductivity. A fit of the conductivity near threshold was extrapolated to determine  $V_{th} = -2.67 \text{ V}$  for sample A and  $V_{th} = -2.73 \text{ V}$  for sample B. Photoresponse measurements presented in the article were performed with  $V_{G2} = -2.80 \text{ V}$  for sample A and  $V_{G3} = -2.80 \text{ V}$  for sample B. Samples A and B were characterized independently and aligned to the terahertz source using a raster scan to locate the maximum photovoltage signal at a given excitation frequency. All measurements were performed at  $T = 8 \text{ K}$ .

Received 11 April 2013; accepted 14 August 2013;  
published online 29 September 2013

## References

- Yablonovitch, E., Gmitter, T. J. & Leung, K. M. Photonic band structure: the face-centered-cubic case employing nonspherical atoms. *Phys. Rev. Lett.* **67**, 2295–2298 (1991).
- Yoshie, T. *et al.* Vacuum Rabi splitting with a single quantum dot in a photonic crystal nanocavity. *Nature* **432**, 200–203 (2004).
- Baba, T. Slow light in photonic crystals. *Nature Photon.* **2**, 465–473 (2008).
- Berrier, A. *et al.* Negative refraction at infrared wavelengths in a two-dimensional photonic crystal. *Phys. Rev. Lett.* **93**, 073902 (2004).
- Yablonovitch, E. Inhibited spontaneous emission in solid-state physics and electronics. *Phys. Rev. Lett.* **58**, 2059–2062 (1987).
- John, S. Strong localization of photons in certain disordered dielectric superlattices. *Phys. Rev. Lett.* **58**, 2486–2489 (1987).
- Allen, S. J., Tsui, D. C. & Logan, R. A. Observation of the two-dimensional plasmon in silicon inversion layers. *Phys. Rev. Lett.* **38**, 980–983 (1977).
- Dyakonov, M. I. & Shur, M. S. Detection, mixing, and frequency multiplication of terahertz radiation by two-dimensional electronic fluid. *IEEE Trans. Electron Dev.* **43**, 380–387 (1996).
- Ju, L. *et al.* Graphene plasmonics for tunable terahertz metamaterials. *Nature Nanotech.* **6**, 630–634 (2011).
- Yan, H. *et al.* Tunable infrared plasmonic devices using graphene/insulator stacks. *Nature Nanotech.* **7**, 330–334 (2012).
- Grigorenko, A. N., Polini, M. & Novoselov, K. S. Graphene plasmonics. *Nature Photon.* **6**, 749–758 (2012).
- Mackens, U., Heitmann, D., Prager, L., Kotthaus, J. P. & Beinvogl, W. Minigaps in the plasmon dispersion of a two-dimensional electron gas with spatially modulated charge density. *Phys. Rev. Lett.* **53**, 1485–1488 (1984).
- Muravev, V. M. *et al.* Tunable plasmonic crystals for edge magnetoplasmons of a two-dimensional electron system. *Phys. Rev. Lett.* **101**, 216801 (2008).
- Dyer, G. C. *et al.* Inducing an incipient terahertz finite plasmonic crystal in coupled two dimensional plasmonic cavities. *Phys. Rev. Lett.* **109**, 126803 (2012).
- Andress, W. F. *et al.* Ultra-subwavelength two-dimensional plasmonic circuits. *Nano Lett.* **12**, 2272–2277 (2012).
- Burke, P. J., Spielman, I. B., Eisenstein, J. P., Pfeiffer, L. N. & West, K. W. High frequency conductivity of the high-mobility two-dimensional electron gas. *Appl. Phys. Lett.* **76**, 745–747 (2000).
- Rana, F. Graphene terahertz plasmon oscillators. *IEEE Trans. Nanotechnol.* **7**, 91–99 (2008).
- Staffaroni, M., Conway, J., Vedantam, S., Tang, J. & Yablonovitch, E. Circuit analysis in metal-optics. *Phot. Nano. Fund. Appl.* **10**, 166–176 (2012).
- Aizin, G. R. & Dyer, G. C. Transmission line theory of collective plasma excitations in periodic two-dimensional electron systems: finite plasmonic crystals and Tamm states. *Phys. Rev. B* **86**, 235316 (2012).
- Shvets, G. & Urzhumov, Y. A. Engineering the electromagnetic properties of periodic nanostructures using electrostatic resonances. *Phys. Rev. Lett.* **93**, 243902 (2004).
- Lemoult, F., Lerosey, G., de Rosny, J. & Fink, M. Resonant metalenses for breaking the diffraction barrier. *Phys. Rev. Lett.* **104**, 203901 (2010).
- Lemoult, F., Fink, M. & Lerosey, G. Acoustic resonators for far-field control of sound on a subwavelength scale. *Phys. Rev. Lett.* **107**, 064301 (2011).
- Liu, Z. *et al.* Locally resonant sonic materials. *Science* **289**, 1734–1736 (2000).
- Davanco, M., Urzhumov, Y. & Shvets, G. The complex Bloch bands of a 2D plasmonic crystal displaying isotropic negative refraction. *Opt. Express* **15**, 9681–9691 (2007).
- Tamm, I. E. Über eine mögliche Art der Elektronenbindung an Kristalloberflächen. *Phys. Z. Sowjetunion* **1**, 733–736 (1932).
- Shaner, E. A. *et al.* Far-infrared spectrum analysis using plasmon modes in a quantum-well transistor. *IEEE Photon. Technol. Lett.* **18**, 1925–1927 (2006).
- Davoyan, A. R., Popov, V. V. & Nikitov, S. A. Tailoring terahertz near-field enhancement via two-dimensional plasmons. *Phys. Rev. Lett.* **108**, 127401 (2012).

28. Smith, D. R., Vier, D. C., Koschny, T. & Soukoulis, C. M. Electromagnetic parameter retrieval from inhomogeneous metamaterials. *Phys. Rev. E* **71**, 036617 (2005).
29. Simovski, C. R. Bloch material parameters of magneto-dielectric metamaterials and the concept of Bloch lattices. *Metamaterials* **1**, 62–80 (2007).
30. Yoon, H., Yeung, K. Y. M., Umansky, V. & Ham, D. A Newtonian approach to extraordinarily strong negative refraction. *Nature* **488**, 65–69 (2012).
31. Ohno, H. *et al.* Observation of 'Tamm states' in superlattices. *Phys. Rev. Lett.* **64**, 2555–2558 (1990).
32. Goto, T. *et al.* Optical Tamm states in one-dimensional magnetophotonic structures. *Phys. Rev. Lett.* **101**, 113902 (2008).
33. Sasin, M. E. *et al.* Tamm plasmon polaritons: slow and spatially compact light. *Appl. Phys. Lett.* **92**, 251112 (2008).
34. Muravev, V. M. & Kukushkin, I. V. Plasmonic detector/spectrometer of subterahertz radiation based on two-dimensional electron system with embedded defect. *Appl. Phys. Lett.* **100**, 082102 (2012).
35. Zhang, S., Genov, D. A., Wang, Y., Liu, M. & Zhang, X. Plasmon-induced transparency in metamaterials. *Phys. Rev. Lett.* **101**, 047401 (2008).
36. Liu, N. *et al.* Plasmonic analogue of electromagnetically induced transparency at the drude damping limit. *Nature Mater.* **8**, 758–762 (2009).
37. Tassin, P., Zhang, L., Koschny, T., Economou, E. N. & Soukoulis, C. M. Low-loss metamaterials based on classical electromagnetically induced transparency. *Phys. Rev. Lett.* **102**, 053901 (2009).
38. Luk'yanchuk, B. *et al.* The Fano resonance in plasmonic nanostructures and metamaterials. *Nature Mater.* **9**, 707–715 (2010).
39. Fowler, R. H. Notes on some electronic properties of conductors and insulators. *Proc. R. Soc. Lond. A* **141**, 56–71 (1933).
40. Shockley, W. On the surface states associated with a periodic potential. *Phys. Rev.* **56**, 317–323 (1939).
41. Totsuka, K., Kobayashi, N. & Tomita, M. Slow light in coupled-resonator-induced transparency. *Phys. Rev. Lett.* **98**, 213904 (2007).
42. Vakil, A. & Engheta, N. Transformation optics using graphene. *Science* **332**, 1291–1294 (2011).
43. Muravjov, A. V. *et al.* Temperature dependence of plasmonic terahertz absorption in grating-gate gallium-nitride transistor structures. *Appl. Phys. Lett.* **96**, 042105 (2010).
44. Chen, J. *et al.* Optical nano-imaging of gate-tunable graphene plasmons. *Nature* **487**, 77–81 (2012).
45. Fei, Z. *et al.* Gate-tuning of graphene plasmons revealed by infrared nano-imaging. *Nature* **487**, 82–85 (2012).
46. Sydoruk, O., Syms, R. R. A. & Solymar, L. Distributed gain in plasmonic reflectors and its use for terahertz generation. *Opt. Express* **20**, 19618–19627 (2012).
47. Dyer, G. C. *et al.* Enhanced performance of resonant sub-terahertz detection in a plasmonic cavity. *Appl. Phys. Lett.* **100**, 083506 (2012).
48. Lissauskas, A. *et al.* Rational design of high-responsivity detectors of terahertz radiation based on distributed self-mixing in silicon field-effect transistors. *J. Appl. Phys.* **105**, 114511 (2009).
49. Preu, S. *et al.* Terahertz detection by a homodyne field effect transistor multiplicative mixer. *IEEE Trans. THz Sci. Technol.* **2**, 278–283 (2012).
50. Klimenko, O. A. *et al.* Temperature enhancement of terahertz responsivity of plasma field effect transistors. *J. Appl. Phys.* **112**, 014506 (2012).

### Acknowledgements

The work at Sandia National Laboratories was supported by the Department of Energy Office of Basic Energy Sciences. This work was performed, in part, at the Center for Integrated Nanotechnologies, a US Department of Energy, Office of Basic Energy Sciences user facility. Sandia National Laboratories is a multi-program laboratory managed and operated by Sandia Corporation, a wholly owned subsidiary of Lockheed Martin Corporation, for the US Department of Energy's National Nuclear Security Administration (contract DE-AC04-94AL85000).

### Author contributions

G.C.D., S.J.A. and E.A.S. conceived and designed the devices. J.L.R. grew the 2DEG material. E.A.S. and D.B. fabricated and imaged the devices. A.D.G. and G.C.D. assembled the experiment. G.C.D. measured and analysed the data. G.R.A. and G.C.D. developed the theory and performed the model computations. G.C.D. wrote the manuscript with editorial input from G.R.A. and E.A.S. All authors discussed the results and commented on the paper.

### Additional information

Supplementary information is available in the online version of the paper. Reprints and permissions information is available online at [www.nature.com/reprints](http://www.nature.com/reprints). Correspondence and requests for materials should be addressed to G.C.D. and E.A.S.

### Competing financial interests

The authors declare no competing financial interests.